

Many-body localization proximity effect in a two-species bosonic Hubbard modelPietro Brighi ¹, Marko Ljubotina ¹, Dmitry A. Abanin ², and Maksym Serbyn ¹¹*Institute of Science and Technology Austria (ISTA), Am Campus 1, 3400 Klosterneuburg, Austria*²*Department of Theoretical Physics, University of Geneva, 24 Quai Ernest-Ansermet, 1211 Geneva, Switzerland*

(Received 11 April 2023; revised 9 June 2023; accepted 27 June 2023; published 4 August 2023)

The many-body localization (MBL) proximity effect is an intriguing phenomenon where a thermal bath localizes due to the interaction with a disordered system. The interplay of thermal and nonergodic behavior in these systems gives rise to a rich phase diagram, whose exploration is an active field of research. In this paper, we study a bosonic Hubbard model featuring two particle species representing the bath and the disordered system. Using state-of-the-art numerical techniques, we investigate the dynamics of the model in different regimes, based on which we obtain a tentative phase diagram as a function of coupling strength and bath size. When the bath is composed of a single particle, we observe clear signatures of a transition from an MBL proximity effect to a delocalized phase. Increasing the bath size, however, its thermalizing effect becomes stronger and eventually the whole system delocalizes in the range of moderate interaction strengths studied. In this regime, we characterize particle transport, revealing diffusive behavior of the originally localized bosons.

DOI: [10.1103/PhysRevB.108.054201](https://doi.org/10.1103/PhysRevB.108.054201)**I. INTRODUCTION**

The concept of a thermal bath plays a central role in the description of equilibrium systems in statistical mechanics. Typically, a bath is defined as a large system, unaffected by the coupling to the system considered, whose role is to provide a reservoir of energy to the system and thermalize it. Recent advances in the field of quantum simulators, however, allow for an unprecedented degree of control over the experimental setup parameters. This has introduced the possibility of studying small quantum baths and their interactions with otherwise isolated quantum systems [1,2]. In this scenario, one can also study the effect of the coupling to the system on the bath itself.

Intuitively, coupling an ergodic system to a bath will result in a combined system with similar properties. However, in the cases where the system is nonergodic and hence does not satisfy the eigenstate thermalization hypothesis [3,4], more exotic phenomena can be observed. A natural question then arises regarding the various phases in these systems and their stability with respect to the model parameters. Examples of nonergodic systems are integrable models [5–7], however, these are known to be unstable to weak perturbations [8]. Thus, the expected outcome is the eventual thermalization of the system through the coupling with the bath, although recent studies have shown that, in special cases, seemingly stable bound states can form [9,10]. A more robust scenario is offered by disordered systems, since the many-body localized (MBL) phase [11–14] arising there represents an example of strong ergodicity breaking stable to weak perturbations,

thus providing an interesting case of study for the fate of non-ergodic systems coupled to baths.

In this scenario, two distinct outcomes are possible. First, similarly to the case of integrable models, the coupling to the bath could lead to the system thermalizing. Alternatively, the quantum bath can be affected by the coupling to the disordered system leading to a breakdown of thermalization in the bath itself, via the so-called MBL proximity effect [15]. Motivated by experiments [1,2] and by the fundamental question of the stability of MBL in the presence of a bath, a large number of works [15–29] considered the interplay of disordered and ergodic systems in different setups. Of these, Refs. [16,17,19,23,25,27] studied the case when the back action of the MBL system onto the bath can be discarded, thus excluding the possibility of an MBL proximity effect. A different setting, where the thermal bath is modeled as an ergodic many-body system, thus being potentially prone to localization due to the interaction with the MBL system, was considered by Refs. [15,18,28,29].

In this context, some recent studies [28,29] provided numerical evidence for the stability of the MBL proximity effect in the special case of a quantum bath consisting of a single particle. The bath-MBL coupling was realized using a Hubbard model with two hard-core bosonic species, inspired by the experimental setup of Ref. [1]. In this model, one of the particle types, the *disordered bosons*, experience a random on-site potential, thus representing a nonergodic localized system. The second species—the *clean bosons*—are not subject to the random on-site potential and play the role of a quantum bath of variable size, depending on the number of such particles. Using matrix product state (MPS) [30] based algorithms for numerical time evolution and for accessing highly excited eigenstates, Refs. [28,29] demonstrated that at strong disorder and strong bath-system coupling, the single clean boson fails to thermalize an extensive number of disordered particles and gets localized by the disorder induced by the interaction with

the localized particles. Despite providing evidence of the realization of the MBL proximity effect, Refs. [28,29] left many open questions. In particular, the fate of the system at weaker interactions and in the case of larger baths (for instance, at a finite density of clean particles) remained unexplored. Moreover, a recent work [31] challenged the conclusions on the stability of localization, hinting at the possibility of delocalization at longer times.

In this paper, we use state-of-the-art numerical methods with large computational resources to consider hitherto inaccessible regimes of the two-species Hubbard model. First, we address the case of a small quantum bath represented by a single clean boson at weak system-bath interaction. Analytical arguments suggest the possibility of a breakdown of the MBL proximity effect in this regime and the delocalization of the clean particle. Numerically, we investigate the time evolution of the model and additionally consider a related Floquet model with similar properties, which enables the study of much longer timescales, as well as the investigation of Floquet-MBL [32–36]. At sufficiently large interaction strengths, we still observe characteristic features of localization, in contrast with the claims of Ref. [31]. Upon decreasing the coupling strength, we observe signatures of delocalization of the clean particle, whereas the disordered bosons still show extremely slow dynamics, making their behavior hard to capture unambiguously.

After establishing the possibility of delocalization of the single-particle bath, we investigate the effects of increasing the size of the quantum bath. Using operator dynamics, we consider the case when the particle density of the bath and of the localized particles are comparable. In this case, we find nonvanishing (diffusive or weakly subdiffusive) particle transport for both clean and disordered bosons, providing strong evidence of delocalization. As the density of the clean particles is reduced, such that their average spacing approaches the localization length of a single clean particle in the case of the MBL proximity effect, we observe dynamics compatible with localization at short times. The rapid growth of entanglement prevents us from reaching longer timescales, where from the analytical treatment of related problems delocalization may be expected [37,38].

By pushing the limits of numerical simulations to large systems, long evolution times, and large entanglement regimes, our work sheds light on the fate of a localized system coupled to a bath with varying number of particles. For a weak quantum bath, we demonstrate the persistence of localization in systems with a much larger number of particles than is accessible to exact diagonalization, suggesting the stability of MBL on long timescales and possibly in the thermodynamic limit [39,40]. In the opposite limit of a large quantum bath, our investigation of transport shows a surprisingly fast emergence of diffusive behavior of the localized system due to its coupling with the bath, in contrast with observations of subdiffusive transport throughout the delocalized phase of more conventional disordered many-body Hamiltonians with a single species of particles [41,42]. This is suggestive of a possible effective long-range interaction induced by the clean bosons, bearing a distant analogy to studies of two-level systems coupled to waveguides that mediate long-range interactions [43].

The paper is structured as follows. In Sec. II, we introduce the model and give a summary of the different methods and regimes studied throughout the paper. We then investigate the case of a quantum bath represented by a single particle, exploring the localization-delocalization transition both numerically and with an analytical approximation in Secs. III A and III B, respectively. Section IV is devoted to the case of a finite density of particles in the bath: We first study transport in the limit of large particle densities in the bath in Sec. IV A and attempt to capture the transition as a function of particle density in the bath in Sec. IV B. Finally, we summarize our results and highlight possible future directions in Sec. V.

II. MODEL

We study a one-dimensional system of hard-core bosons (also referred to as spinless fermions in the literature) featuring two different particle types. Disordered bosons, or d bosons, are subject to a random on-site potential $\epsilon_i \in [-W, W]$ and are thus *Anderson localized* in the absence of interactions [44,45]. Clean bosons (c bosons) instead have no on-site potential, with hopping amplitude t_c , and represent the *bath*. The two-particle species are then coupled through a Hubbard-type density-density local interaction, leading to the full Hamiltonian

$$\hat{H} = t_d \sum_i (\hat{d}_{i+1}^\dagger \hat{d}_i + \text{H.c.}) + \sum_i \epsilon_i \hat{n}_{d,i} + t_c \sum_i (\hat{c}_{i+1}^\dagger \hat{c}_i + \text{H.c.}) + U \sum_i \hat{n}_{c,i} \hat{n}_{d,i}, \quad (1)$$

where $\hat{n}_{c,i} = \hat{c}_i^\dagger \hat{c}_i$, and $\hat{n}_{d,i} = \hat{d}_i^\dagger \hat{d}_i$. In our numerical simulations, we will consider the system with open boundary conditions with a system size chosen sufficiently large to ensure the absence of finite size effects (see Appendix A 2 for details). The model has $U(1) \times U(1)$ symmetry due to the simultaneous particle conservation of both bosonic species. This results in a block-diagonal structure of the Hamiltonian, with the dimension of each block determined by $\dim(\mathcal{H}) = \mathcal{C}_{N_d}^L \mathcal{C}_{N_c}^L$, with $N_{c/d} = \sum_i \hat{n}_{c/d,i}$ being the total particle number, L the system size, and \mathcal{C}_n^m the binomial coefficient.

Throughout this paper, we study the dynamics numerically using both continuous Hamiltonian time evolution and pulsed Floquet driving. The Hamiltonian evolution is generated by the unitary time-evolution operator $\hat{U}(t) = \exp(-i\hat{H}t)$, implemented numerically using a fourth-order Suzuki-Trotter decomposition [46] over alternating pairs of sites with a time step $\delta t = 0.05$. The Floquet dynamics, instead, are generated by the following time-dependent periodic Hamiltonian:

$$\hat{H}(t) = \begin{cases} \hat{H}_{\text{even}} & nT_F \leq t < (n+1/2)T_F \\ \hat{H}_{\text{odd}} & (n+1/2)T_F \leq t < (n+1)T_F, \end{cases} \quad (2)$$

where $\hat{H}_{\text{even(odd)}}$ represents the Hamiltonian in Eq. (1). Here the sum of the hopping terms is restricted to even (odd) sites, the interaction and disorder terms are halved, $T_F = 0.5$ is the period, and $n \in \mathbb{N}$. The unitary Floquet operator

$$\hat{U}_F = e^{-i\hat{H}_{\text{odd}}T_F/2} e^{-i\hat{H}_{\text{even}}T_F/2} \quad (3)$$

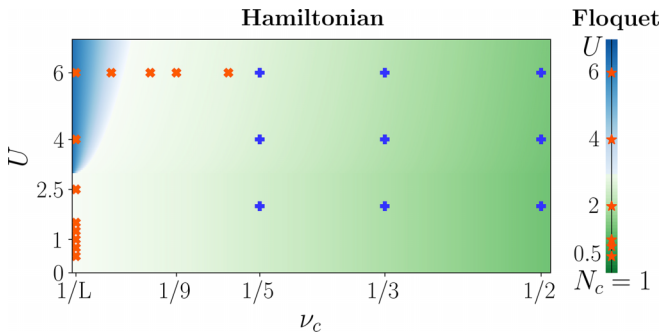


FIG. 1. The phase diagram for the Hamiltonian system as function of the coupling U and the bath size ν_c , and for the Floquet dynamics in the case of bath consisting of a single particle ($N_c = 1$ or $\nu_c = 1/L$). The markers show different points in parameter space explored in this paper, and refer to time evolution that uses Hamiltonian or Floquet (red markers) propagation of wave functions and Hamiltonian evolution of density matrices (blue crosses). The colors schematically show the different phases, blue representing MBL and green the ergodic phase. The shading corresponds to the putative transition regime, obtained from our numerical simulations. Based on previous studies, we expect more stable localization in the regime of strong interactions, however, in the present paper we deliberately choose interactions smaller than the disorder strength, $U < W = 6.5$.

then describes the dynamics at *stroboscopic times* nT_F . Although the Hamiltonian and Floquet models are, strictly speaking, different, the Floquet dynamics is expected to reduce to the Hamiltonian case in the limit of $T_F \rightarrow 0$. Moreover, both models are characterized by the *exact conservation* of the particle numbers of the two bosonic species. This allows us to compare the transport and particle spreading between the two models. As we demonstrate below, Floquet and Hamiltonian time evolution show similar phenomenology, with Floquet time evolution enabling us to probe the stability of MBL proximity effect and delocalization on much longer timescales at a comparable computational cost.

To address different regimes in the parameter space of the model, we investigate the dynamics of two different types of initial conditions. Whenever the density of clean bosons is small, $\nu_c = N_c/L \leq 1/6$, we fix the d boson density to $\nu_d = 1/3$ and study the evolution of the quantum wave function represented as an MPS from an initial state consisting of clean (disordered) bosons forming a density wave of period $1/\nu_{c(d)}$, respectively. Our numerical simulations show that, upon increasing the density of clean particles in the bath, the whole system approaches thermalization, thus leading to rapid entanglement spreading and making the time evolution of the MPS wave function extremely challenging. Thus, in the regime of $\nu_c > 1/6$ we time evolve density matrices initialized close to infinite temperature ($\rho_\infty \propto \mathbb{1}$) represented as a matrix product operator (MPO), whose simulation is more efficient in the thermal phase; see Appendix B for details.

In Fig. 1, we summarize the main results of this paper through a tentative phase diagram as a function of interaction strength U and bath size controlled by the density of clean particles, ν_c , for fixed parameters $t_c = t_d = 1$ and $W = 6.5$ used in previous works to ensure a short localization length of d bosons $\xi_d \lesssim 1$ [28,29]. We consider interactions to be

of order or smaller than disorder strength. This restriction may disfavor the localized phase that is expected to be more stable at strong interaction, but at the same time it avoids the presence of very different energy scales in the problem.

In Sec. III, we study the transition as a function of the interaction strength for the single-particle bath case, expanding our previous work [28,29] to a hitherto unexplored regime. The joint results of our numerical simulations and analytical considerations allow us to establish the existence of two phases in this regime, an MBL phase at strong interactions (blue in the phase diagram) and a thermal phase at weak U (light green), characterized by diffusive behavior of the bath particle and extremely slow relaxation of the d bosons. In this part of our paper, we use both Hamiltonian and Floquet dynamics, presenting qualitatively similar results.

As the number of c bosons becomes extensive, $N_c \propto L$, corresponding to finite densities of clean bosons, we observe, in Sec. IV, a weakening of localization, eventually yielding delocalization shown as a crossover from blue to green in the phase diagram in Fig. 1. Finally, as ν_c is increased, we further investigate particle transport deep in the delocalized region of the diagram, finding diffusive spreading of both bosonic species.

III. BATH CONSISTING OF A SINGLE CLEAN BOSON

We first investigate our model in the case of a bath composed of a single clean boson, $N_c = 1$. As already shown in Refs. [28,29], at strong interactions the disordered bosons induce localization of the small bath. Here we address the presence of a transition to the thermal phase as the interaction strength is decreased, using both quasiexact large-scale numerical simulations and analytical considerations.

A. Numerical evidence for a phase transition

Using a highly efficient parallel implementation of the time-evolving block decimation (TEBD) algorithm [47] with a large bond dimension $\chi = 5000$ and small truncation error $\varepsilon = 10^{-9}$, we simulate the dynamics generated by the Hamiltonian Eq. (1) in large systems of $L = 252$ sites. This choice of parameters, together with the fourth-order Suzuki-Trotter decomposition with a small time step ($\delta t = 0.05$), guarantees almost exact numerical results up to the times when bond dimension saturates. We further explore Floquet dynamics of MPSs of maximal bond dimension $\chi = 2048$ and systems with up to $L = 2000$ sites. The large system sizes studied and the long timescales achieved in our work allow us to exclude boundary effects due to the finite size of the system and reach the high entanglement regime. As we shall demonstrate below, this is particularly important in the weak interaction case due to the delocalization and spreading of the clean boson to large distances.

In both the Hamiltonian and Floquet cases, we focus on the dynamics of an initial product state corresponding to a d boson (\bullet) density wave of period $1/\nu_d = 3$ and a single clean boson (\circ) initialized in the middle of the system at site $i = L/2$:

$$|\psi_0\rangle = \underbrace{|\bullet \circ \circ \bullet \circ \circ \dots \bullet \circ \circ\rangle}_{1/\nu_d} \circ \dots \bullet \circ \circ \dots \bullet \circ \circ \rangle. \quad (4)$$

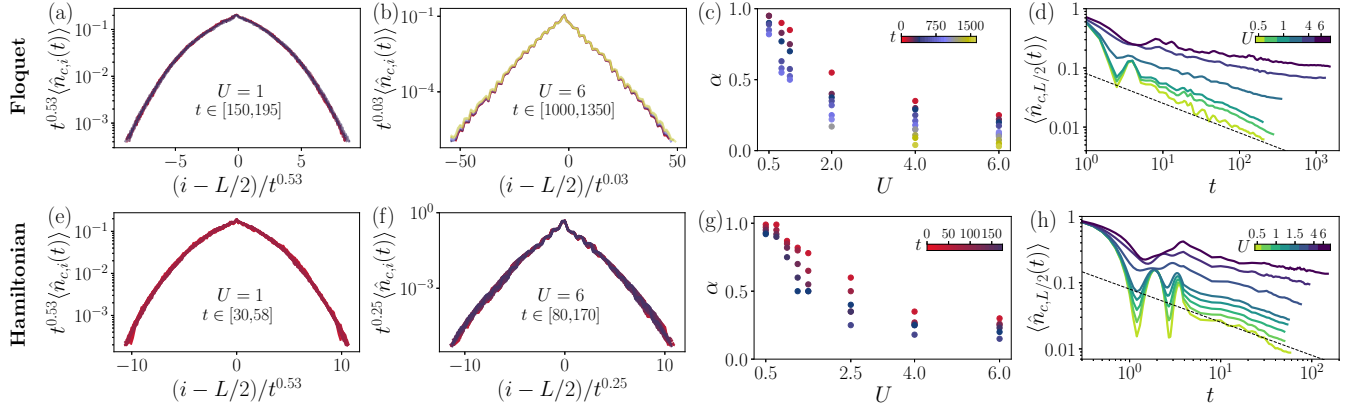


FIG. 2. In the top row, we show data for the Floquet model. (a) At $U = 1$, the density profiles at long times $150 \leq t \leq 200$ collapse when rescaling the space axis by \sqrt{t} , indicating diffusive behavior of the c boson. (b) At $U = 6$, a similar collapse of the density profile is obtained with a much smaller exponent $\alpha = 0.03$, a value that could be consistent with zero, suggesting localization. (c) The exponent $\alpha(U)$ as a function of interaction strength U shows that diffusive spreading of the c boson at weak interactions $\alpha \approx 1/2$ slows down and becomes localized at strong U as witnessed by $\alpha \rightarrow 0$. The color scale indicates the time range used to obtain the exponent; range of accessible times is limited at weak U by entanglement growth. (d) Decay of the c boson density at its original site $i = L/2$ is consistent with $1/\sqrt{t}$ (black dashed line) in the delocalized phase, and it shows signatures of saturation at strong interaction $U \geq 4$. The bottom row shows similar data but for Hamiltonian dynamics limited to shorter times. (e) Hamiltonian dynamics show a similar behavior indicating diffusion of the c boson at weak interaction. (f) At larger U , density profiles collapse with a larger exponent α than in the Floquet case. This can be attributed to the shorter times achieved in Hamiltonian dynamics, as Floquet dynamics show comparable values of α at earlier times, see panels (g) and (h). The system size is $L = 2000$ for Floquet and $L = 252$ for Hamiltonian dynamics, data are averaged over ten disorder realizations.

The choice of this initial state allows us to sample the behavior of typical states where the clean boson is far from the boundaries and is surrounded by a sea of d bosons of approximately uniform density.

1. Diffusive behaviors of the bath at weak interaction

We analyze the behavior of the clean particle that constitutes the bath by studying the evolution of its density profile $\langle \hat{n}_{c,i}(t) \rangle = \langle \psi(t) | \hat{n}_{c,i} | \psi(t) \rangle$ with time. In the localized and ergodic phases, the bath spreading is expected to show very different characteristic properties. When the c boson gets localized through the MBL proximity effect, the density profile decays exponentially away from the initial position and the localization length is expected to saturate at long times. In contrast, when the MBL proximity effect fails to localize the bath, the clean boson is expected to spread diffusively due to the influence of the disordered system, hence showing a Gaussian density profile with the density at the original site decaying as $\propto 1/\sqrt{t}$.

To characterize the dynamics of the c boson, we perform collapses of its density profile at different times, using the following scaling form:

$$\langle \hat{n}_{c,i}(t) \rangle = t^{-\alpha} f\left(\frac{i - L/2}{t^\alpha}\right). \quad (5)$$

The value of the exponent $\alpha(U)$ can be thought of as a proxy for the inverse dynamical exponent and is used to distinguish the diffusive and localized behavior of the bath. These density profile collapses are shown in Figs. 2(a) and 2(b) for Floquet dynamics and in Figs. 2(e) and 2(f) for Hamiltonian evolution. At weak interaction strength $U = 1$, the value of $\alpha \approx 0.5$ in both the Hamiltonian and Floquet cases suggests a delocalized bath. Conversely, the Floquet model at strong interaction $U = 6$ exhibits a vanishing exponent $\alpha \approx 0$ high-

lighting the saturation of the c boson spreading and suggesting the persistence of the MBL proximity effect already observed at stronger interactions [28,29]. In the Hamiltonian time evolution, however, the exponent α is still decaying and attains a larger value that can be ascribed to the shorter times achieved in this regime. Indeed, a comparison with the collapse in the corresponding time window of the Floquet evolution results in a good agreement of the value of α as shown in Fig. 2(c), suggesting that at later times the exponent will eventually decay also in the Hamiltonian case.

In addition to different values of α obtained from the rescaling, the density profiles of the clean boson in Figs. 2(a), 2(b), 2(e), and 2(f) also have a qualitatively different form. In the delocalized phase, the boson density shows a characteristic Gaussian profile as opposed to the exponential decay observed at strong interactions.

The study of exponent α at different times and as a function of U is presented in Figs. 2(c) and 2(g). Saturation towards $\alpha = 1/2$ is observed at $U < 2$, and is especially apparent for Floquet evolution. For Hamiltonian dynamics, the values of the exponent remain close to $\alpha = 1$ at times $t \approx 150$. This suggests that a much longer time evolution is needed to see the crossover to diffusion. In contrast, for $U \geq 2.5$ the value of α decreases with increasing evolution time. This hints at a possible transition from delocalization to localization occurs in the window of interaction strengths $1 \lesssim U \lesssim 2.5$. Due to the fast entanglement growth observed in it, this critical region is also the most challenging to treat numerically, thus preventing a more accurate estimate of the transition point. The transition in the behavior of the bath can also be captured by the different dynamics of the central site density decaying as $\approx 1/\sqrt{t}$ in the delocalized case and saturating to a finite value at strong U , as shown in Figs. 2(d) and 2(h). Note that the saturation of the density in the Floquet dynamics for $U = 2$ in

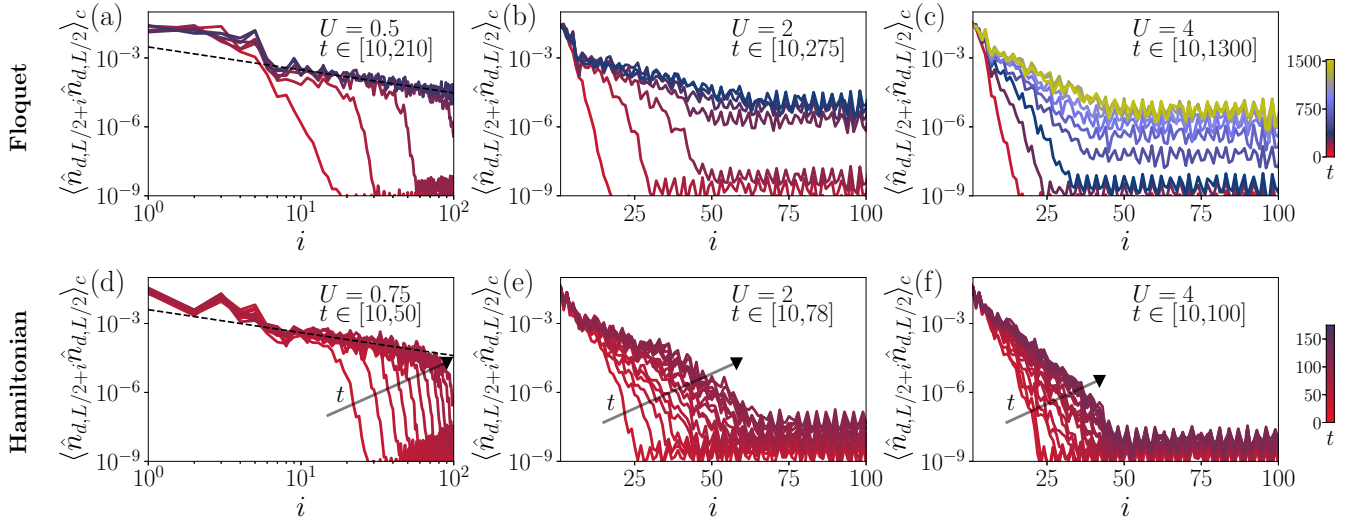


FIG. 3. Density-density connected correlation functions for d bosons in Floquet (a)–(c) and Hamiltonian (d)–(f) time evolution. At weak interactions, (a) and (d), correlations decay algebraically with distance, consistent with $1/i$ dependence (black dashed line). Such algebraic decay of connected correlation functions suggests delocalization of d bosons on long timescales. As U is increased, however, the localized behavior is eventually recovered, and (c) and (f) show exponentially decaying correlation functions for $U = 4$. We notice the emergence of a plateau far from $i = L/2$ in the Floquet case, which is due to the truncation error arising from the faster saturation of bond dimension in this type of time evolution. Data are averaged over ten disorder realizations for system size $L = 2000$ and $L = 252$ for the Floquet and Hamiltonian systems, respectively.

Fig. 2(d) at long times may suggest that the bath is localized at this interaction strength, at the timescales accessible to our simulations. Finally, in Appendix A 3 we provide further evidence of the c boson transition by showing a diverging decay length at $U < 2$.

2. Slow delocalization of disordered bosons

Due to the small bath size, changing the interaction strength U has a much weaker influence on the density profiles of d bosons. Indeed, comparing the density profiles and the imbalance at different values of U naïvely suggests that the disordered particles remain localized for all values of interaction strength, at least at the accessible timescales. A deeper investigation of more sensitive probes, provided by the entanglement entropy and the connected correlation functions of d bosons, however, reveals the existence of two contrasting behaviors at weak and strong U .

As shown in Appendix A 4, the global half-chain entanglement entropy grows algebraically for small values of the interaction, characterized by a universal behavior $S_{L/2}(t) \propto (tU^\beta)^\gamma$, with $\gamma \approx 0.39$ and $\beta \approx 1.1$ in the Floquet case. In the Hamiltonian case, a qualitatively similar picture holds, although the value of β suddenly drops to ≈ 0.6 as $U > 1$. This deviation from the logarithmic growth of the entanglement entropy indicates that the system cannot be fully localized. The analysis of the entanglement profile provides further evidence in favor of delocalization, as its growth is not limited to the central part of the chain but propagates to regions far from the initial position of the clean particle.

To further probe the behavior of the d bosons, we analyze their density-density connected correlations,

$$\langle \hat{n}_{d,i} \hat{n}_{d,j} \rangle_c = \langle \hat{n}_{d,i} \hat{n}_{d,j} \rangle - \langle \hat{n}_{d,i} \rangle \langle \hat{n}_{d,j} \rangle, \quad (6)$$

shown in Fig. 3 [Floquet (a)–(c), Hamiltonian (d)–(f)] as a function of the distance from the center and at different times. At weak interactions below the transition $U < U_c$, the connected correlations present a slow $1/|i - j|$ decay in space (black dashed line) and spread in time to regions far from the center, confirming the slow delocalization of the d bosons. On the other hand, in the MBL proximity effect phase, density correlations decay exponentially, with a decay length slowly increasing in time and eventually saturating, as highlighted by the collapse of the curves at late times. For values of $U \geq 4$, we notice that the decay length of the d boson correlations, $\ell_d(t)$, seems to saturate to a value comparable with the length scale of the exponential suppression of the c boson density, $\ell_c(t)$. Note that the saturation value of $\ell_{c,d} \approx 5$ obtained for $U = 4$ is much smaller than the simulated system size, thus hinting at the localization of c and d bosons.

In conclusion, our large-scale numerical simulations reveal two qualitatively different behaviors in the system at large and weak interaction strengths. Such distinction would be difficult to make in smaller systems where the finite size affects the spreading of both particle types. In the regime of large U , both boson species are localized. At weak U , while we observe a spreading of c bosons over the distances of hundreds of lattice sites, the dynamics of d bosons are much slower, and we are unable to fully determine their fate despite reaching long times $t \geq 200$ in our simulations.

B. Estimating the critical coupling from mapping to a Bethe lattice

After identifying numerically the existence of two different phases, we construct a phenomenological picture of the transition that allows to obtain analytical estimates. To analyze

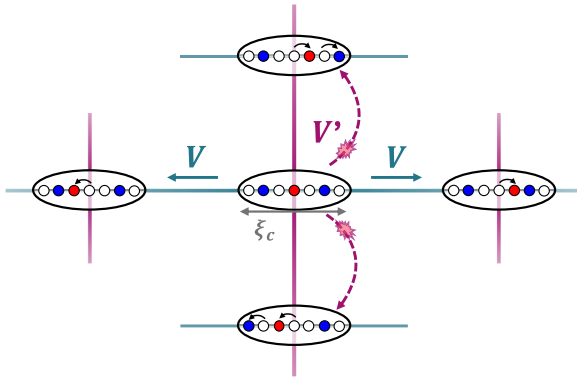


FIG. 4. Schematic representation of the Bethe lattice, where a small $K = 4$ is chosen for clarity. Each node represents a different boson configuration in Fock space. *Elastic* scattering (horizontal edges) connects nodes where only the c boson moves with a hopping amplitude V . The simultaneous hopping of clean and disordered bosons instead gives rise to *inelastic* processes (vertical edges) with amplitude V' .

the behavior of our model in the weak interaction regime, we first consider the Hartree picture presented in Ref. [29], where both the bath and d bosons are localized with localization length $\xi_c \gtrsim 10 \gg \xi_d$ ¹ at weak coupling. The Anderson orbitals $\{|\alpha\rangle\}$ form a complete basis that we use to rewrite the particle creation and annihilation operators $\hat{d}_i^\dagger = \sum_\alpha \phi_\alpha(i) \hat{d}_\alpha^\dagger$, with $\phi_\alpha(i) = \langle \alpha | i \rangle \approx \exp(-|i - x_\alpha|/\xi_\alpha) / \sqrt{2\xi_\alpha}$. The interaction then corresponds to simultaneous c and d bosons hopping among different localized orbitals:

$$U \sum_i \hat{n}_{c,i} \hat{n}_{d,i} = \sum_{\alpha\beta\gamma\delta} V_{\alpha\beta}^{\gamma\delta} \hat{d}_\alpha^\dagger \hat{d}_\beta \hat{c}_\gamma^\dagger \hat{c}_\delta. \quad (7)$$

In particular, we focus on the motion of the clean boson comprising the quantum bath. The hopping between different orbitals, arising from the interaction term in Eq. (7), can be depicted on a graph representing the Fock space. Each node in this graph corresponds to a certain filling of localized orbitals and edges connect different configurations with the matrix element obtained from Eq. (7). While long-range hoppings are allowed, they are exponentially suppressed due to the localization of both particle species in the Hartree limit. Therefore, neglecting the edges connecting configurations where the particles move farther than their localization length, we approximate the full Fock space as a graph of connectivity $K \approx \xi_c^2 \xi_d v_d (1 - v_d)$, where the $v_d(1 - v_d)$ term accounts for the finite density of d bosons and their hard-core nature (see Ref. [29] for detailed derivation).

A second, crucial, approximation corresponds to neglecting all loops in the graph, resulting in a Bethe lattice with coordination number K , as shown pictorially in Fig. 4 for $K = 4$. In this graph, we distinguish two types of hopping

processes for the clean boson, *elastic* and *inelastic*. In *elastic* hoppings, the c boson moves without changing the pattern of occupation of d boson orbitals, i.e., $\alpha = \beta$ in Eq. (7). These processes, depicted by solid arrows in Fig. 4, correspond to the motion of the clean particle in the random environment created by the d bosons. Alternatively, the c boson motion can simultaneously produce a scattering of the d boson from one orbital to another. We refer to this second type of process as *inelastic* and represent it as dashed arrows in Fig. 4.

A phenomenological mapping of the motion of the c boson to a finite coordination number Bethe lattice allows us to use the results of Abou-Chacra *et al.* [49] and obtain a condition for the stability of localization. The stability of the localized phase is controlled by the interplay of the disorder strength on the lattice \mathcal{W} , the connectivity K , and the matrix element of the hopping processes, V . Reference [49] derives a transcendental equation for the critical value of the matrix element V_c , $\frac{2KeV_c}{\mathcal{W}} \ln\left(\frac{\mathcal{W}}{2V_c}\right) = 1$, such that the localized phase is stable for $V < V_c$. To apply this result to our model, we estimate the typical matrix element V , the disorder strength \mathcal{W} , and the connectivity K . To establish the typical matrix element V , we first consider its approximate expression

$$V_{\alpha\beta}^{\gamma\delta} \approx \frac{U}{\xi_c \xi_d} \sum_i e^{-\frac{|i-x_\alpha|+|i-x_\beta|}{\xi_d}} e^{-\frac{|i-x_\gamma|+|i-x_\delta|}{\xi_c}}, \quad (8)$$

where we replace the orbital-specific localization length with its average and neglect the oscillatory part of the wave function. In Appendix A 5, we estimate the typical value of V , which in the case of $\xi_c \gg \xi_d \approx 1$ can be approximated as $V \approx U/(2\xi_d)$. Finally, using the estimate for the connectivity $K \approx \xi_c^2 \xi_d v_d (1 - v_d)$ [29], we can estimate the transition by numerically solving the equation for the critical hopping amplitude on the Bethe lattice at fixed $t_c = t_d = 1$ and $W = 6.5$. In the Hartree approximation, the effective disorder results from the interaction with the d bosons, and is thus proportional to the coupling strength, $\mathcal{W} \propto U$. Also, the localization length of the c boson scales as $\xi_c \propto U^{-2}$ [29]. Thus, the decrease of the hopping amplitude at weak U is counteracted by a larger effective connectivity and weaker effective disorder, leading to instability of localization below a certain critical value of interaction strength. The numerical estimate suggests that in this parameter range, localization becomes unstable at a critical value of the coupling $U_c \approx 3$, in good agreement with the transition window inferred from the numerical results of Sec. III A.

In summary, the phenomenological mapping of the hopping of the single clean boson to the Bethe lattice discussed above predicts an instability of localization at sufficiently weak interactions U in agreement with our numerical simulations. The present approach differs from the method used previously in Ref. [29], where the ratio of the typical matrix element to the level spacing was used as a criterion for delocalization. While the resulting critical curves are qualitatively similar, we expect the current mapping to the Bethe lattice to be more accurate in the weak coupling regime. Indeed, in the present paper we focus primarily on the behavior of the c boson in the case of $\xi_c \gg \xi_d \approx 1$, where the problem can be interpreted as a weakly localized single particle occasionally perturbed by the inelastic scattering of d bosons. Additionally,

¹Note that the large localization length of the c boson could potentially give rise to *avalanches* [48] which would delocalize the entire chain. Nevertheless, such delocalization within the avalanche mechanism is expected to occur on timescales that exceed the reach of current simulations.

considering the motion of the c boson in the Bethe lattice gives an intuitive explanation of the diffusive behavior observed in Sec. III A. In the standard picture of single-particle localization on the Bethe lattice, the motion of the particle in the delocalized phase is ballistic, since the majority of the steps increase the distance of the particle to the origin. In contrast, our mapping naturally reproduces diffusion in the delocalized phase, since at each point half of the hopping processes move the c boson to the left and the remaining half moves it to the right, see Fig. 4 for a schematic picture.

In the case of finite density of c bosons, we expect the approximation to the Bethe lattice presented above to break down due to the relevant presence of loops. Discarding them can lead to inaccurate conclusions favoring delocalization due to the fact that loops correspond to quantum interference whose effect is typically to enhance localization. Understanding if the present phenomenological mapping to the Bethe lattice is capable of reproducing other aspects of numerical simulations, such as entanglement dynamics or very slow relaxation of d bosons in the delocalized phase, remains an interesting open question.

IV. EXTENSIVE BATH

In the previous section, we provided evidence of a transition between regimes of localized and delocalized small baths tuned by the interaction strength, U . In this section, we study the effect of increasing the density of c bosons that constitute the bath to a finite value. First, in Sec. IV A we consider the case when the density of c bosons is close to half filling, and investigate particle transport. Afterward, we study the regime of finite but small density of clean bosons in Sec. IV B.

A. Particle transport at large clean boson density

We first approach the regime where the clean particles have a large overall density $v_c \geq 1/5$. In this regime, we expect that the bath triggers delocalization of the d bosons. To characterize the resulting delocalized phase, we study the transport of bosons using the time evolution of density matrices close to infinite temperature represented as MPOs. This has several advantages over simulating states directly, which we discuss in Appendix B.

Following a well-established approach [50], we initialize the system in a density matrix characterized by a small step in the center of the particle density profile. Figure 5 illustrates such an initial density profile, with density in the left (right) part of the chain being set to $v_{c(d)} \pm \mu_{c(d)}$. This condition translates to an initial density matrix written as a tensor product of density matrices on individual sites. The density matrix of individual site of c bosons (and, analogously, d bosons) can be written as

$$\rho_c^{(i)} = \begin{pmatrix} 1 - v_c - \mu_c(i) & 0 \\ 0 & v_c + \mu_c(i) \end{pmatrix}, \quad (9)$$

where $\mu_c(i) = \pm 0.01$ in the left and right halves, respectively. Since the time evolution of density matrices represented as MPOs is most efficient when they are close to infinite temperature, we fix the d boson density to be $v_d = 1/2$. We then apply operator TEBD to large chains of $L = 100$ sites up to

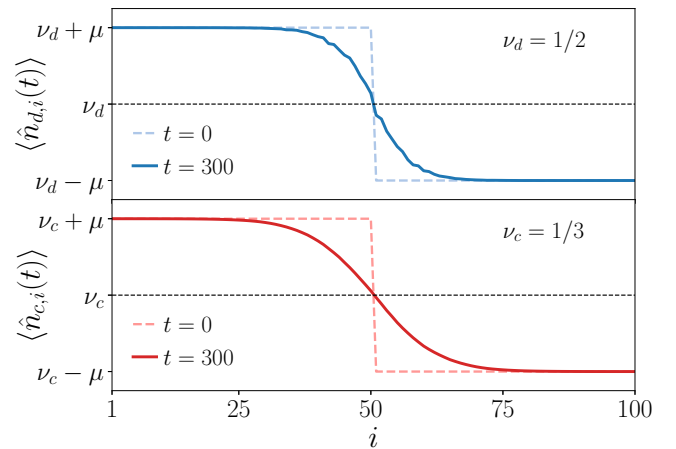


FIG. 5. Density profile of disordered and clean bosons at late (solid lines) and initial (dashed lines) times. The small density step of magnitude 2μ slowly melts due to the particle current running from the left to the right part of the chain. Data are shown for $U = 6$, $W = 6.5$, and averaged over 30 disorder realizations.

times $T = 300$, using a maximal bond dimension in the range $\chi \in [128, 192]$, depending on the convergence of the results, shown in Appendix B 1.

To characterize particle transport, we study the evolution of the transferred particle number, $\delta n_{c(d)}(t)$, defined as the difference between the density profile at zero time and time t , $\langle \hat{n}_{c(d),i}(t) \rangle$:

$$\delta n_{c(d)}(t) = \sum_{i=1}^{L/2} [\langle \hat{n}_{c(d),i}(0) \rangle - \langle \hat{n}_{c(d),i}(t) \rangle]. \quad (10)$$

The change of density with time corresponds to the current across the central site, integrated over time, thus quantifying the transport of particles. In particular, the logarithmic derivative of $\delta n_{c(d)}$ with respect to time can be related to the instantaneous inverse dynamical exponent $1/z(t)$:

$$\frac{1}{z(t)} = \frac{d \ln \delta n(t)}{d \ln t}. \quad (11)$$

We study the particle flow as a function of interaction strength U and density of particles in the bath, v_c . As we show in Fig. 6, $\delta n_{c(d)}(t)$ at times larger than $t \geq 10$ has a clear power-law behavior for both particle species, confirming the delocalization of the originally Anderson localized d bosons due to the coupling to the bath. However, the fact that d bosons without coupling to the bath are localized is reflected by the qualitatively different behavior of the transported number of particles with changing U apparent in Figs. 6(a) and 6(b). With increasing interaction strength, the c bosons exhibit slower transport, whereas the d bosons are characterized by faster transport.

In Figs. 6(c)–6(f), we show the instantaneous dynamical exponent $z_{c(d)}(t)$ extracted using Eq. (11). We report results for two different particle densities in the bath, $v_c = 1/2$ in Figs. 6(c)–6(e) and $v_c = 1/3$ in Figs. 6(d)–6(f), at different coupling strengths U . Figures 6(e) and 6(f) show that the transport features of the bath are unaffected by the variation of the bath particle density and interaction strength, U , with

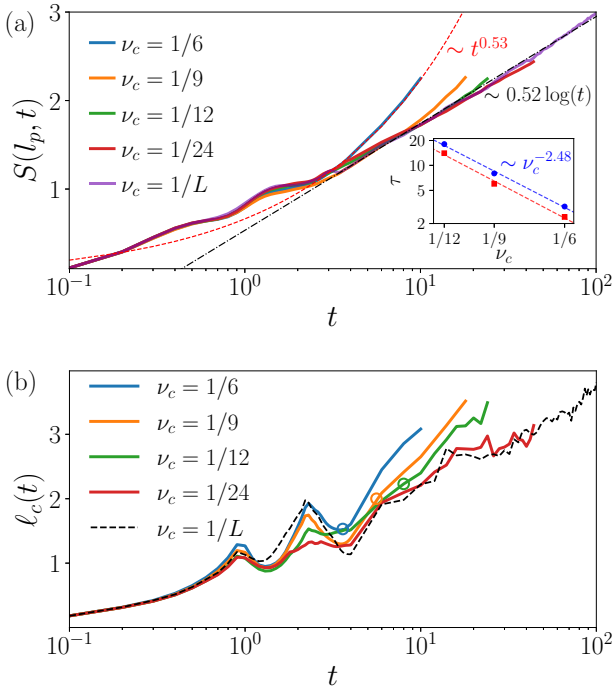


FIG. 7. (a) Entanglement entropy across a cut between sites l_p and $l_p + 1$, where $\langle \hat{n}_{c,l_p}(t=0) \rangle = 1$ for all the densities studied. For densities $\nu_c \geq 1/12$, we observe a deviation at a time $\tau_S(\nu_c)$ from the curve corresponding to the case of a single c boson (purple line). In the inset, we show the behavior of this characteristic timescale as a function of density, suggesting a power-law behavior. Comparison of τ obtained from the entanglement entropy (blue dots) and the one obtained from the growth of the correlation functions (red squares) suggests that both timescales behave in a similar way. (b) The decay length $\ell_c(t)$ averaged among all c bosons composing the bath also deviates from the decay length of a single clean boson (black dashed line) at late times for $\nu_c \geq 1/12$.

so it can accommodate an extensive number of clean bosons. We further choose a large system size $L = 126$ such that even at the smallest density, $\nu_c = 1/24$, the bath hosts a significant number of clean bosons, $N_c = 5$.

In Appendix B 3, we report on the behavior of density profiles and imbalance, confirming delocalization at large ν_c characterized by relaxation of the initial density wave pattern. At smaller bath densities, however, signatures of thermalization are absent up to timescales $T \approx 50$. To capture the transition, then, we analyze the behavior of a more sensitive probe—entanglement entropy.

Since entanglement growth is influenced by the distance to the closest c boson, we compare bipartite entanglement across a cut l_p such that $\langle \hat{n}_{c,l_p}(t=0) \rangle = 1$ for all considered densities of clean bosons. This comparison is shown in Fig. 7(a), together with the entanglement entropy relative to the bath consisting of a single clean particle. After an initial transient logarithmic regime, entanglement entropy eventually curves upwards, indicating a faster power-law growth with time. We observe such deviation from the single-particle case for all values $\nu_c \geq 1/12$ and track its characteristic onset time $\tau_S(\nu_c)$. The scaling of $\tau_S(\nu_c)$ is shown in the inset of Fig. 7(a). Within the considered range of densities, the be-

havior of $\tau_S(\nu_c)$ is consistent with a power-law increase at low ν_c , $\tau_S(\nu_c) \propto 1/\nu_c^{-2.48}$, that implies eventual delocalization at any finite density of clean bosons. Of course, the limited data range does not allow us to rule out the possibility that $\tau_S(\nu_c)$ diverges at a finite value of ν_c , signaling stability of localization at a finite density of clean bosons.

The analysis of the density-density correlation functions of the c bosons shown in Appendix B 3, provides a possible explanation for the power-law entanglement growth. We notice that the correlations among two initially occupied sites l_p and l'_p become relevant at a timescale scaling with the bath density with the same power-law exponent observed for τ_S , as shown by the red line in the inset of Fig. 7(a). The agreement between the scaling of the two timescales implies that the faster entanglement growth is triggered only when c boson correlations become significant. As a consequence of the strong suppression of the spreading of the clean boson degrees of freedom, when ν_c is small enough correlations may saturate to a very small value compatible with the logarithmic growth of entanglement, thus possibly leading to a localized phase even at a finite density of clean bosons.

Deviations from single-particle behavior can also be observed in the time evolution of the c boson density profiles. In particular, we probe this by studying the decay length $\ell_c(t)$ of each individual c boson obtained by fitting the density profile in the vicinity of each l_p to the ansatz proposed in Ref. [28]:

$$n_c(x, t) = \mathcal{N}_c(t) \exp\left(-\frac{|x|}{\ell_c(t) \tanh\left(\frac{R(t)}{|x|}\right)}\right). \quad (13)$$

Here $\mathcal{N}_c(t)$ is a time-dependent normalization factor and $R(t)$ describes the Gaussian part of the profile emerging at small densities. In the present case, we average the results for $\ell_c(t)$ obtained for each clean boson. As shown in Fig. 7(b), at early times the decay length behaves in agreement with the single-particle case for all densities ν_c (note that the deviations from the dashed curve can be attributed to the additional averaging for finite ν_c). At later times marked by circles, however, the decay length grows consistently faster than in the case of an intensive bath for all bath sizes $\nu_c \geq 1/12$.

While the scaling of τ shown in the inset of Fig. 7(a) seems to suggest thermalization at all finite ν_c , the potential localization of the individual c bosons indicated by the agreement of the decay length for $\nu_c = 1/24$ with the single c boson curve might lead to a breakdown of the delocalization mechanism at small, albeit extensive, bath sizes. Unfortunately, on the timescales available to our numerical simulations, we are not able to confirm that the $\nu_c = 1/24$ bath leads to power-law growth of entanglement or to deviations in the growth of $\ell_c(t)$. Using the power-law fit for $\tau_S(\nu_c)$, we can estimate that the deviation from logarithmic growth at small bath size would take place at a time $T \approx 100$, corresponding to a nearly uniform entanglement entropy $S \geq 3$ —an extremely challenging regime in TEBD simulations.

V. DISCUSSION

Our work highlights physical aspects of localization that can be studied using multispecies lattice models. While considering the mixture of two hard-core bosons severely impacts

the system sizes reachable with exact diagonalization techniques, it presents a smaller limiting factor for the highly efficient MPS-based numerical simulations employed here. In the present case, considering the two-species model resulting in a mixture of disordered and clean particles allowed us to show the stability of the MBL proximity effect [15]. Besides the persistence of localization at strong coupling, we also presented evidence of a transition driven by the interaction strength. Decreasing the interaction leads to delocalization and diffusion of the clean particle, together with a slow inhomogeneous relaxation of the disordered bosons.

In addition, we explored the presence of a phase transition tuned by the density of clean bosons. Our study of transport highlights that at large densities of clean particles the system is delocalized. The investigation of the putative delocalization transition at small but finite density of clean bosons, however, is not conclusive due to the rapid entanglement growth preventing our simulation from reaching sufficiently late times. Thus, further studies are needed to understand if there exists a finite critical density of clean particles below which the entire system stays localized [15] or whether delocalization occurs at any finite density of clean particles akin to scenario suggested by Refs. [37,38].

Numerous other questions remain open. In particular, although the single clean particle spreads diffusively at weak interactions, the disordered bosons show extremely slow relaxation. Such behavior is intuitively similar to the delocalized yet nonergodic phase suggested to exist on Bethe lattices [54–56]. It remains to be understood if our phenomenological mapping of the two-species Hubbard model to the Bethe lattice can reproduce the relaxation of disordered bosons, entanglement dynamics, and other physical properties, such as the behavior of connected correlation functions. More broadly, the delocalization of a single particle atop the infinite sea of localized bosons presents a deviation from the standard thermodynamic limit, where typically densities of all particle species are assumed to be finite. Building a theory of the delocalization transition for such a system remains an interesting challenge. Furthermore, the role of interactions between disordered particles as well as the nature of disorder (random or quasiperiodic) provide a complementary set of control parameters that was not explored in this paper.

In a different direction, the consideration of finite density of clean particles allows for a standard thermodynamic limit, but turns out to be an extremely challenging problem for numerical simulations. In this regime, although we were able to confirm delocalization at large densities of clean particles, the intermediate density regime proved to be hard to access due to rapid entanglement growth. Understanding the structure of this entanglement and searching for a quasilocal basis transformation may potentially assist one in reaching longer simulation times. This may be crucial for getting insights into microscopic processes and the structure of resonances created by the clean particles that drive the delocalization of the entire system. Additionally, further investigation of the diffusive transport at large densities of particles in the bath may provide useful insights for a better understanding of the subdiffusion observed in standard disordered models used to study MBL [41,42,51].

Finally, modern experiments with ultracold atoms motivate the study of other geometries and setups for the many-body localization proximity effect. In particular, the study involving the two-dimensional cold atom microscope [1] that inspired our paper calls for an extension of our results to two-dimensional systems. While simulating dynamics with two-dimensional tensor network ansatzes is extremely challenging, the study of the present model on ladders with MPS methods may provide useful insights into the qualitative difference between one- and two-dimensional systems [57]. Likewise, large-scale numerical studies of models where the coupling between the localized system and the bath is local [2] may provide useful insights for the theory of MBL and its potential instabilities known as bubbles or avalanches [19,48,58,59].

ACKNOWLEDGMENTS

We thank A. A. Michailidis and A. Mirlin for insightful discussions. P.B., M.L., and M.S. acknowledge support by the European Research Council (ERC) under the European Union’s Horizon 2020 research and innovation program (Grant Agreement No. 850899). D.A. was supported by the European Research Council (ERC) under the European Union’s Horizon 2020 research and innovation program (Grant Agreement No. 864597) and by the Swiss National Science Foundation. P.B., M.L., and M.S. acknowledge PRACE for awarding us access to Joliot-Curie at GENCI@CEA, France, where the TEBD simulations were performed. The TEBD simulations were performed using the ITensor library [60].

APPENDIX A: INTENSIVE BATH

In the main text, we showed numerical results suggesting the existence of a transition to a delocalized phase as the interaction strength between the bath and the disordered particles is decreased. In this Appendix, we provide some additional numerical results for the dynamics of the bath, of the d bosons, and of the system as a whole.

1. Evaluation of the accuracy of TEBD simulations

Due to the finite bond dimension χ and the finite truncation error ε , the wave function evolved using the TEBD algorithm $|\psi_\chi(t)\rangle$ deviates from the true state $|\psi(t)\rangle$. The error produced by the truncation of the singular values λ_a and corresponding Schmidt states, however, is well controlled and can be easily evaluated. At each singular value decomposition, the local weight of the wave function lost is given by

$$\epsilon_n = \sum_{\lambda_a < \varepsilon} \lambda_a^2 \quad \text{or} \quad \epsilon_n = \sum_{a > \chi} \lambda_a^2, \quad (\text{A1})$$

depending on whether the bond dimension at the evaluated link is saturated or not.

The global error at each time step, then, corresponds to

$$\epsilon(t) = 1 - |\langle \psi(t) | \psi_\chi(t) \rangle|^2 = 1 - \prod_n (1 - \epsilon_n). \quad (\text{A2})$$

The total discarded weight at the end of the time evolution finally amounts to the integrated error $\epsilon(t)$.

In the work presented in the main text, we used extremely large bond dimensions and a low truncation error, thus ensuring the accuracy of our simulations. In the Hamiltonian case, we set $\chi = 5000$ and $\varepsilon = 10^{-9}$, resulting in a maximum truncation error of $\epsilon = 2 \times 10^{-5}$ arising close to the putative transition, at $U = 1.25$. In the Floquet simulations, we use a smaller bond dimension $\chi = 2048$ and the same truncation as for the Hamiltonian evolution. This gives rise to a maximum error of $\epsilon = 8 \times 10^{-3}$, again at interaction strength $U = 1$ in the vicinity of the transition.

2. System size comparison

In the main text, we reported results for the largest systems studied in our paper, $L = 252$ and $L = 2000$ for Hamiltonian and Floquet models, respectively. In both cases, the density of the c boson never reaches the boundaries of the system at the timescales investigated, thus ensuring the absence of boundary effects. To show that the finite size of the system is negligible in our simulations, we report the comparison of

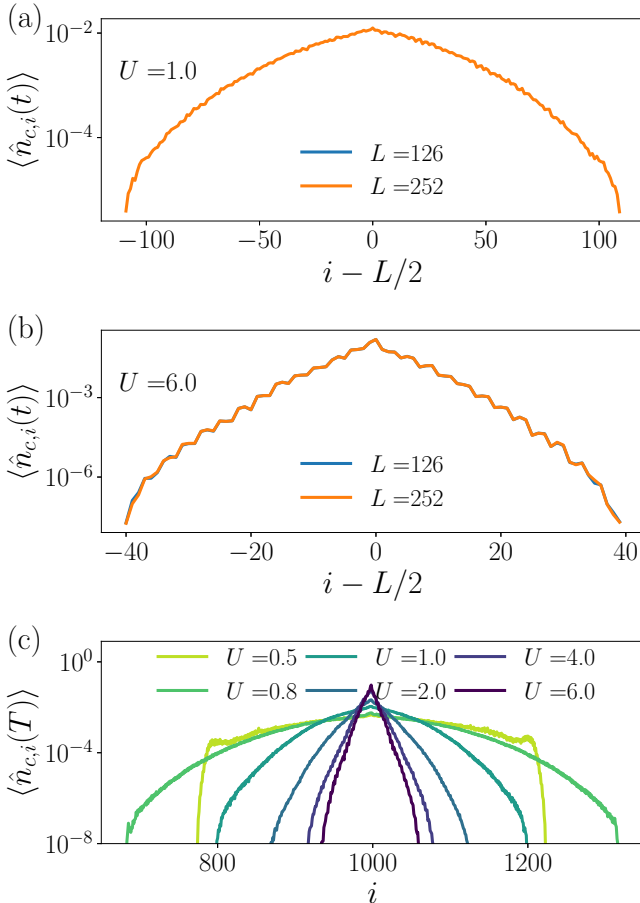


FIG. 8. The c boson density at times $t = 56$ and $t = 100$ for the Hamiltonian evolution at $U = 1$ (a) and $U = 6$ (b). Comparison of two system sizes shows near perfect agreement, confirming the absence of finite-size effects. Panel (c) shows the density profile for different interaction strengths at the respective latest time reached in the Floquet time evolution ($t \in [210, 1600]$). The c boson never reaches the edges of the system, thus ensuring that there are no finite size effects.

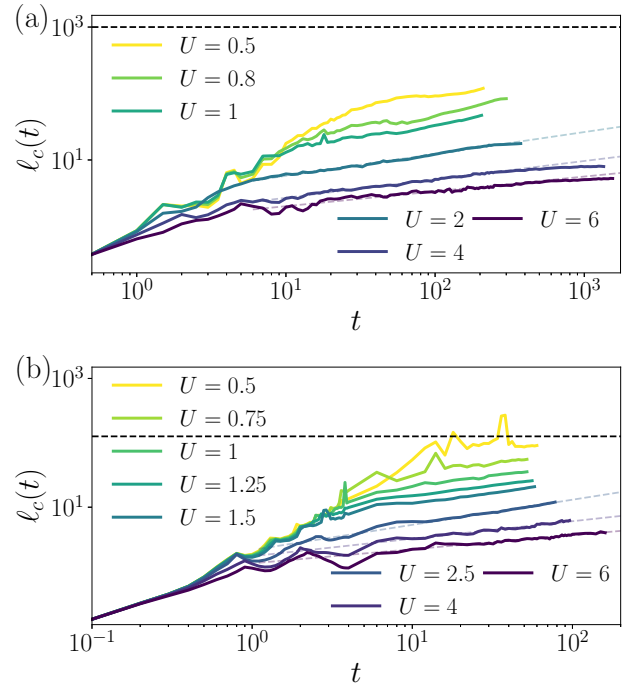


FIG. 9. Clean boson decay length $\ell_c(t)$ shows different behaviors at weak and strong interactions both in the Floquet (a) and Hamiltonian (b) time evolution. At small values of U , below the estimated transition, $\ell_c(t)$ grows persistently with no signs of saturation, reaching the value of half system size $L/2 = 126$ for the Hamiltonian dynamics (black dashed line). As the interaction is increased, the decay length first grows as a power law in time (shaded dashed lines), but eventually, at the long timescales accessible in Floquet evolution, starts saturating. This saturation suggests the potential stability of localization at large U .

two different system sizes $L = 252$ and $L = 126$ in Fig. 8. As reported in Fig. 8, the late time ($t = 56$ and $t = 100$ for $U = 1$ and $U = 6$, respectively) density of the c boson is not affected by the system size. Similarly, in the Floquet model the c boson never approaches the boundary for all the interaction strengths.

3. Additional evidence of bath delocalization

In Sec. III A, we studied the density profile of the clean boson, highlighting the stark difference at weak and strong interactions. We now use the ansatz for the density introduced in Ref. [28],

$$n_c(x, t) = \mathcal{N}_c(t) \exp\left(-\frac{|x|}{\ell_c(t) \tanh\left(\frac{R(t)}{|x|}\right)}\right), \quad (\text{A3})$$

to study the behavior of the decay length $\ell_c(t)$ as the interaction is changed.

In Fig. 9, the dynamics of the decay length is presented for both the Floquet (a) and the Hamiltonian (b) models. The data show a continuous increase of the value of $\ell_c(t)$ as interaction is decreased, in agreement with the transition predicted. In particular, the decay length shows signatures of saturation to a value much smaller than the system size for $U \geq 2$ and $U \geq 4$ in the Floquet and Hamiltonian dynamics, respectively.

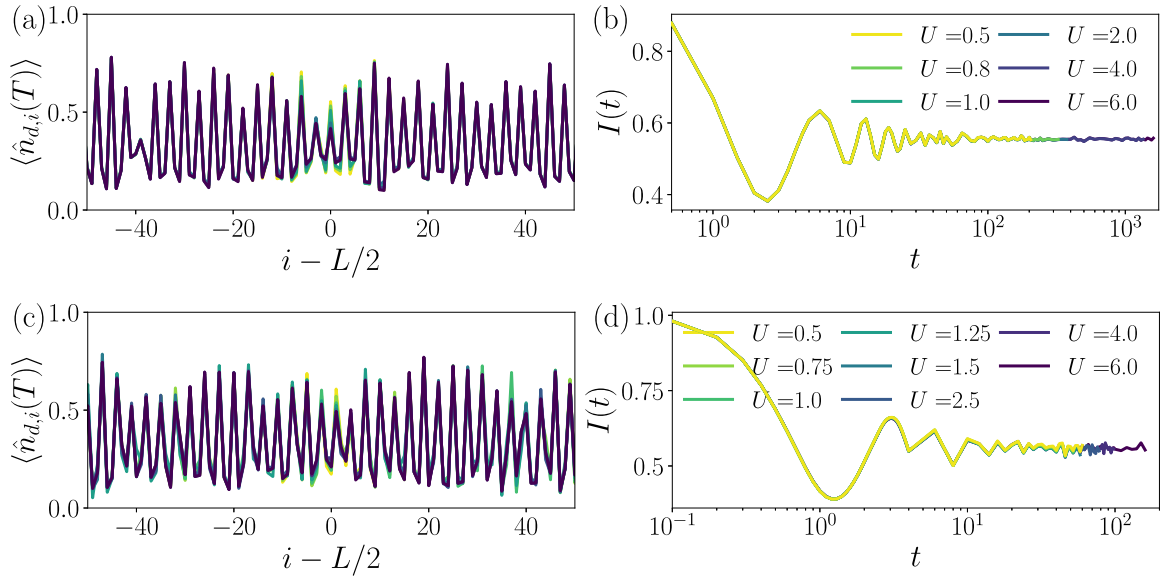


FIG. 10. Late time d boson density profiles [shown for the latest common time among different values of U , $T = 205$, and $T = 54$ for Floquet (a) and Hamiltonian (c) dynamics, respectively] show very weak dependence on the interaction strength. The slight enhancement of relaxation at the center of the chain at large U is caused by the increased effect of localized c bosons on disordered particles. The dynamics of imbalance $I(t)$ in (b) [Floquet] and (d) [Hamiltonian] also illustrates nearly complete absence of density pattern relaxation.

At weaker interactions, instead, it keeps growing, which is suggestive of delocalization.

4. Disordered boson imbalance and global entanglement

Due to the vanishing density of the bath particle in the extremely large systems we study, its effect on the d boson density is weak and hard to capture from the study of their density alone. However, in Sec. III A we demonstrate that a study of the density-density connected correlations allows one to observe a qualitative change in the behavior of the disordered particles at weak interactions.

We now show numerical results concerning the density profiles and the relative imbalance to highlight the necessity of studying more complicated operators, such as the connected correlations, and entanglement entropy, to distinguish the behavior of the system at weak and strong interactions. In Figs. 10(a)–10(c), we show the d boson density profiles in Floquet (Hamiltonian) dynamics at late times $T = 205$ ($T = 54$), respectively. A monotonously enhanced relaxation is observed close to the central site $i = L/2$ as the interaction increases. This observation that the density of localized bosons is more affected by the clean particle at strong interactions (when the clean particle is localized) is readily explained by the fact that the confinement of the clean boson to a smaller region helps to relax the density pattern of disordered particles within the localization volume. Far from the center of the chain, however, no significant variation is observed as the interaction strength is changed.

A more quantitative understanding can be obtained from the study of the imbalance [61,62],

$$I(t) = \frac{N_o(t) - N_e(t)}{N_o(t) + N_e(t)}, \quad (\text{A4})$$

where $\hat{N}_{o/e}$ represent the density in the initially occupied/empty sites. For a period $1/\nu_d = 3$ density wave, they read

$$\hat{N}_o = \sum_{i=1}^{L/3} \hat{n}_{d,3i-2}, \quad \hat{N}_e = \frac{1}{2} \sum_{i=1}^{L/3} (\hat{n}_{d,3i} + \hat{n}_{d,3i-1}). \quad (\text{A5})$$

As imbalance measures the *memory* of the initial condition, its vanishing implies delocalization. However, as can be seen in Figs. 10(b)–10(d), both in Floquet and Hamiltonian dynamics the imbalance does not show any sign of decay on the accessible timescales, irrespective of the interaction strength. This suggests that the relaxation of the d bosons quantified by their density pattern is extremely slow.

The study of the entanglement entropy

$$S(i, t) = -\text{tr} \rho_A(t) \ln \rho_A(t), \quad (\text{A6})$$

where the chain is split into two subsystems $A = [1, i]$, $B = [i + 1, L]$, and we consider density matrix $\rho_A(t) = \text{tr}_B |\psi(t)\rangle \langle \psi(t)|$, provides further evidence in favor of the existence of a transition. In many-body localized systems, entanglement entropy is expected to grow logarithmically [63,64], hence a deviation from the logarithmic behavior can be interpreted as a breakdown of MBL. As we show in Figs. 11(a)–11(c) entanglement entropy at weak interactions shows faster than logarithmic behavior, suggesting thermalization. In particular, this leads to a universal power-law scaling of entanglement given by $S \approx (tU^\beta)^\gamma$ with the value of $\gamma \approx 0.39$ for both Floquet (a) and Hamiltonian (b) cases. The value of β is similar between the two models $\beta \approx 1.1$, however, only for $U \leq 1$. For larger values of U up to 1.5, β stays the same in the Floquet case and abruptly changes to $\beta \approx 0.6$ (not shown) in the Hamiltonian case. The universal behavior is captured by the collapse of the different

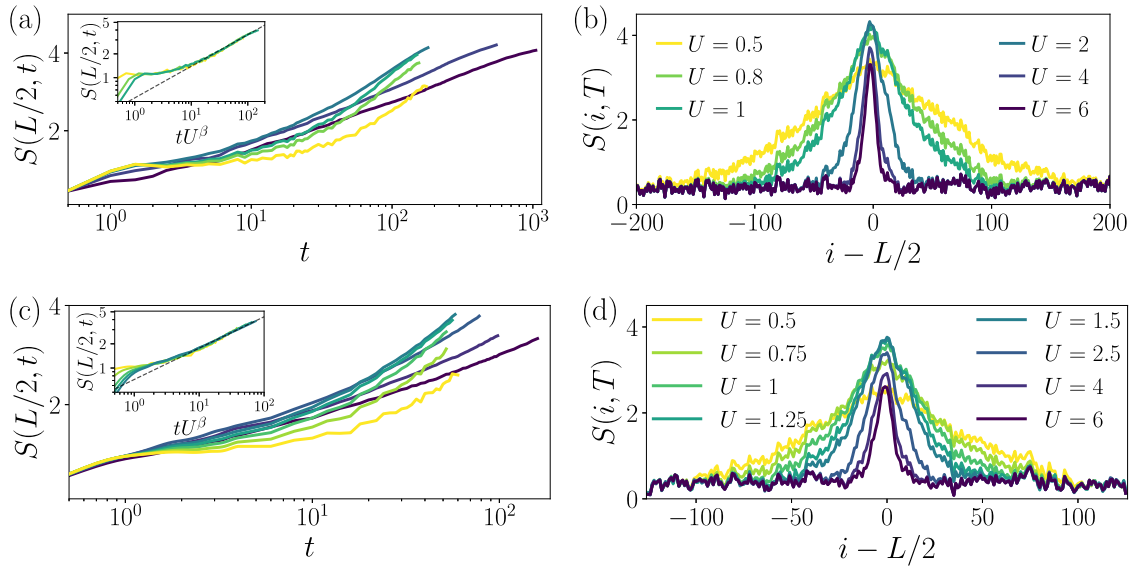


FIG. 11. Dynamics of entanglement entropy show signatures of delocalization for weak coupling U both in Floquet (a), (b) and Hamiltonian (c), (d) dynamics. The power-law growth of entanglement across the central cut shown in (a)–(c) at weak coupling is clearly distinct from the logarithmic behavior observed for $U \geq 4$. The different behavior is also highlighted by the entanglement collapse shown in the inset, suggesting a universal power-law behavior in the ergodic phase. The behavior of real-space entanglement profiles at a fixed time [$T = 205$ for Floquet (b) and $T = 52$ for Hamiltonian dynamics (d)] in (b)–(d) also shows nonmonotonic behavior, with a peak in the region $U \in [1, 2]$ separating two distinct regimes. At weaker interactions, entanglement spreads more uniformly through the chain, suggesting the presence of a large ergodic region close to the center. In contrast, at strong coupling, entanglement growth remains limited to the center of the chain, in agreement with the phenomenology of the MBL proximity effect [28].

entanglement curves shown in the inset of Figs. 11(a)–11(c). As the interaction strength increases, logarithmic growth is eventually restored at $U = 4, 6$, in agreement with MBL.

The different behavior is also highlighted by the spatial profile of entanglement, i.e., the entanglement entropy shown as a function of the size of subsystem A at a fixed time T [$T = 205$ in Fig. 11(b) and $T = 52$ in Fig. 11(d)]. Figures 11(b)–11(d) show that at strong interactions, entanglement growth is limited to the center of the chain, in agreement with the phenomenology proposed in Ref. [28]. At weaker interactions, entanglement starts spreading more uniformly through the chain, indicating the creation of large ergodic regions in the chain. Interestingly, this phenomenon gives rise to a nonmonotonicity of the peak of the entanglement profile as a function of interaction strength. At very weak interactions, entanglement spreads to far regions, and in turn its value in the center is lower than at intermediate U , where its spreading is reduced. We observe a maximum of the peak around $U \approx 2$ in the Floquet case and $U \approx 1.5$ in the Hamiltonian dynamics, which could correspond to the transition point, separating the two entanglement regimes. The value U at which we observe the largest entanglement appears to be stable with respect to the fixed time T for all accessible times $T > 10$.

5. Hopping matrix element for effective mapping to Bethe lattice

In the main part of the text, we used the approach of Ref. [49] to estimate the critical interaction strength separating the localized and ergodic phases. In this Appendix, we detail the evaluation of the typical matrix element, crucial in estimating the transition. As mentioned in the text,

the functional form of the matrix element Eq. (8) depends on the relative position of the different particles involved in the process. In particular, they can be either *mixed*, i.e., $dcdc, dccd, cdcd, cddc$, or they can be *ordered*, corresponding to $ddcc, ccdd$.

Let us first consider the mixed case and analyze the case $cdcd$ in detail. We define the different positions of the particles as $x_{c,d}^{(1,2)}$, where the numerical indices represent the ordering from left to right. It will be useful to define the distance among same type particles $r_{c(d)} = x_{c(d)}^{(2)} - x_{c(d)}^{(1)}$ and the center of mass $\bar{x}_{c(d)} = (x_{c(d)}^{(2)} + x_{c(d)}^{(1)})/2$. In this setup, we identify three different regions: region I: $j \leq x_d^{(1)}$, region II: $x_d^{(1)} < j < x_c^{(2)}$, and region III: $j \geq x_c^{(2)}$. In region I, the summand is $f(j) \leq e^{-r_c/\xi_c} e^{-2(\bar{x}_d - j)/\xi_d}$; in region II $f(j)$ is constant and attains its maximal value $f(j) = e^{-r_c/\xi_c - r_d/\xi_d}$; finally, in region III, $f(j) \leq e^{-r_d/\xi_d} e^{-2(j - \bar{x}_c)/\xi_c}$. Consequently, the sum in Eq. (8) can be split into three terms

$$V \leq \frac{U}{\xi_c \xi_d} \left[e^{-r_c/\xi_c} \sum_{j \leq x_d^{(1)}} e^{-2(\bar{x}_d - j)/\xi_d} + e^{-r_c/\xi_c - r_d/\xi_d} (d_{cd} - 2) + e^{-r_d/\xi_d} \sum_{j \geq x_c^{(2)}} e^{-2(j - \bar{x}_c)/\xi_c} \right], \quad (\text{A7})$$

where we introduce $d_{cd} = x_c^{(2)} - x_d^{(1)}$ as the distance between the two middle particles.

The two sums now can be rewritten, introducing a geometric series

$$\begin{aligned} \sum_{j \leq x_d^{(1)}} e^{-2(\bar{x}_d - j)/\xi_d} &= \sum_{j \leq x_d^{(1)}} e^{-(r_d - 2(j - x_d^{(1)}))/\xi_d} \\ &= e^{-r_d/\xi_d} \sum_{k \geq 0} e^{-2k/\xi_d} = \frac{e^{-r_d/\xi_d}}{1 - e^{-2/\xi_d}}. \end{aligned} \quad (\text{A8})$$

A similar approach can be used for the second sum in Eq. (A7). The matrix element for the case of $cdcd$ configuration can thus be estimated to be

$$V \approx \frac{U}{\xi_c \xi_d} e^{-r_d/\xi_d - r_c/\xi_c} \left[\frac{1}{1 - e^{-2/\xi_d}} + (d_{cd} - 2) + \frac{1}{1 - e^{-2/\xi_c}} \right]. \quad (\text{A9})$$

With a similar approach, we can also obtain the upper bound for the matrix element in the remaining cases of mixed bosons, leading to the same result for the $dcdc$ case and to

$$V \approx \frac{U}{\xi_c \xi_d} e^{-r_d/\xi_d - r_c/\xi_c} \left[\frac{2}{1 - e^{-2/\xi_{c(d)}}} + (d_{cc(dd)} - 2) \right] \quad (\text{A10})$$

for the $dccd$ ($cddc$) cases. We numerically check that, in most cases, the bound is reasonably tight, yielding a very small percentage difference from the actual value. We now consider the case of ordered particles. In this case, the summand $f(j)$ is peaked at the position of the middle boson with shorter localization length. Again, for the sake of clarity, we illustrate a particular configuration, but an analogous approach can be used for the other configurations. We choose to show the results for the case $ddcc$ where the localization length of d bosons is shorter than the one of the c boson (the most typical case). In this setup, we can identify two different regions: region I, $j \leq x_d^{(2)}$, where $f(j) \leq e^{-r_d/\xi_d} e^{-2(\bar{x}_c - j)/\xi_c}$, and region II, $j > x_d^{(2)}$, where $f(j) \leq e^{-2(j - \bar{x}_d)/\xi_d - 2(\bar{x}_c - j)/\xi_c}$. The matrix element in region I is upper bounded by

$$\begin{aligned} V^{(I)} &\leq \frac{U}{\xi_c \xi_d} e^{-r_d/\xi_d} \sum_{j \leq x_d^{(2)}} e^{\frac{2j - x_c^{(1)} - x_c^{(2)}}{\xi_c}} \\ &= \frac{U}{\xi_c \xi_d} e^{-r_d/\xi_d - r_c/\xi_c - 2d_{dc}/\xi_c} \sum_{j \leq x_d^{(2)}} e^{\frac{2(j - x_d^{(2)})}{\xi_c}} \\ &= \frac{U}{\xi_c \xi_d} \frac{e^{-r_d/\xi_d - r_c/\xi_c - 2d_{dc}/\xi_c}}{1 - e^{-2/\xi_c}}. \end{aligned} \quad (\text{A11})$$

In region II we obtain

$$\begin{aligned} V^{(II)} &\leq \frac{U}{\xi_c \xi_d} \sum_{j \geq x_d^{(1)} + 1} e^{\frac{-2j + x_d^{(1)} + x_d^{(2)}}{\xi_d}} e^{\frac{2j - x_c^{(1)} - x_c^{(2)}}{\xi_c}} \\ &= \frac{U}{\xi_c \xi_d} e^{-\frac{r_d + 2}{\xi_d}} e^{-\frac{r_c + 2d_{dc} - 2}{\xi_c}} \sum_{k \geq 0} e^{-2\frac{\xi_c - \xi_d}{\xi_c \xi_d} k} \\ &= \frac{U}{\xi_c \xi_d} \frac{e^{-\frac{r_d + 2}{\xi_d}} e^{-\frac{r_c + 2d_{dc} - 2}{\xi_c}}}{1 - e^{-2\frac{\xi_c - \xi_d}{\xi_c \xi_d}}}. \end{aligned} \quad (\text{A12})$$

The case for $\xi_c < \xi_d$ can be obtained in the same way, bearing in mind that now $f(j)$ is peaked at $j = x_c^{(1)}$ and yields the same results as Eqs. (A11) and (A12), except with subscripts

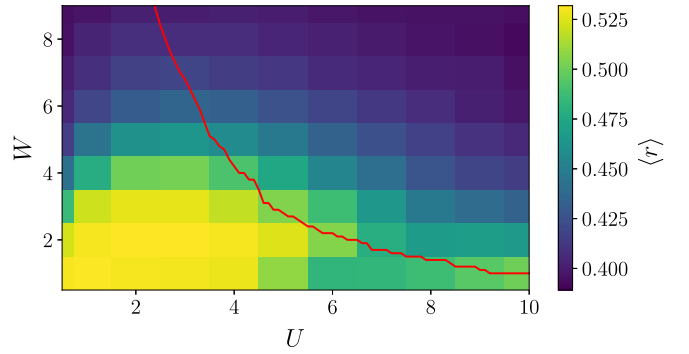


FIG. 12. The critical curve obtained from solving Eq. (A13) numerically (red line) compared with the level spacing ratio for a small $L = 15$ system. Our analytical approach predicts a transition at a critical interaction strength $U_c \approx 3$ for the disorder $W = 6.5$ used in the numerical simulations. This estimate is compatible with the transition window suggested by the results of our large-scale numerical simulations.

for c and d bosons exchanged. A similar statement is valid for the case of $ccdd$ ordered bosons.

Now the estimate of the typical matrix element corresponds to evaluating the average distances $r_{c(d)}$ and d_{cd} , which results in $\langle r_{c(d)} \rangle \approx \xi_{c(d)}/2$ and $d_{cd} \approx \min(\xi_c, \xi_d)$. Finally, using the localization length obtained numerically in the Hartree approximation [29] and solving the equation for the critical point

$$\frac{2KeV_c}{W} \ln\left(\frac{W}{2V_c}\right) = 1 \quad (\text{A13})$$

numerically, we draw the critical line shown in red in Fig. 12. In the heat map, we additionally show results for the average level spacing ratio $\langle r \rangle$ [53,65] obtained from exact diagonalization of the Hamiltonian Eq. (1) on $L = 15$ sites. From this approximate analysis, we extract a critical value of the coupling $U_c \approx 3$ for the disorder strength $W = 6.5$ used throughout this paper. This result is somewhat counter-intuitive, given that the hopping amplitude is proportional to the interaction, $V \propto U$. Nevertheless, as already obtained in a previous work [29], the effective disorder for the c boson is proportional to the coupling strength, and hence its localization length $\xi_c \propto U^{-2}$. This results in the observed trend yielding delocalization at weak U and localization at strong interactions.

APPENDIX B: EXTENSIVE BATH

When studying the behavior of the model with a finite density of c bosons, we employ two distinct approaches. At relatively low densities, we use MPS simulations with the c bosons initially equidistant to one another. However, at higher densities this approach will lead to a prohibitively fast growth of entanglement entropy, which slows down numerical simulations and prohibits us from reaching long timescales. To avoid this issue, we employ an MPO-based approach at large densities around half filling, where we simulate the dynamics of the system's density matrix. In particular, we prepare an initial density matrix with a small step in the c and d boson densities, which can be written as a trivial MPO with bond

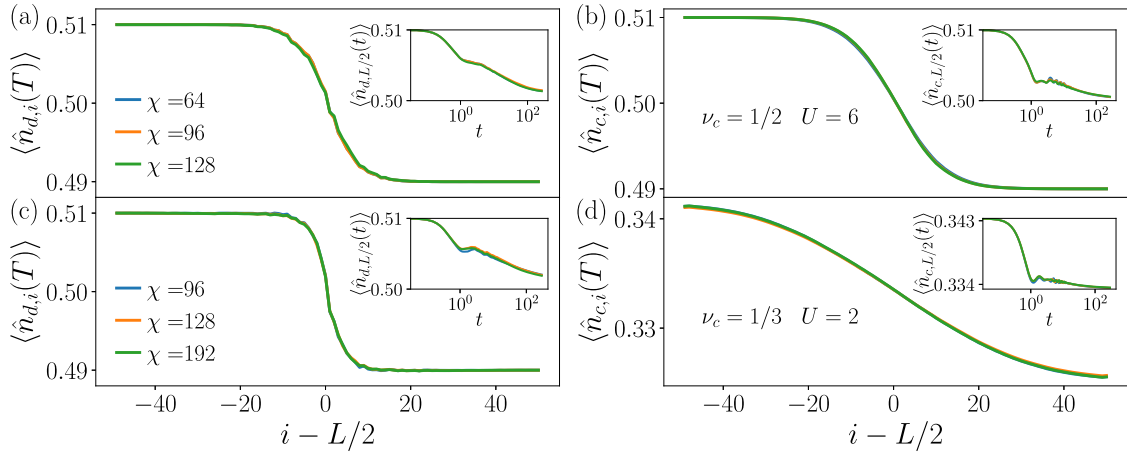


FIG. 13. Bond dimension comparison for two exemplary values of the interaction strength and density, $U = 6$, $\nu_c = 1/2$ in (a), (b) and $U = 2$, $\nu_c = 1/3$ in (c), (d). The main panels show the density profiles for d and c bosons at the latest time $T = 300$, confirming the convergence of our results for the bond dimensions used. Additionally, in the insets we compare the time evolution of the density at the central site, which also shows good convergence with increasing bond dimension.

dimension one. Provided that the local boson density remains near half filling (such as $1/2$ or $1/3$), this initial density matrix leads to relatively slow growth of operator space entanglement entropy (as was also observed in an earlier work [50]). This allows us to reach the timescales necessary to extract information on the transport properties of our model at a high density of c bosons.

1. Bond dimension comparison for density matrix TEBD

To estimate the accuracy of our simulations, we compare the value of certain observables throughout time evolution for different bond dimensions. In Fig. 13, we present the different density profiles of the d bosons and the bath for different values of the interaction and different sizes of the bath. In the top row, we show $U = 6$ and $\nu_c = 1/2$, while Figs. 13(c) and 13(d) present $U = 2$ and $\nu_c = 1/3$. The density profiles at $T = 300$, shown in the main panels, are converged at the bond dimensions used in the simulations presented in the main text. Additionally, in the insets we plot the time evolution of the density at the central site for different bond dimensions, similarly showing converged dynamics at the largest bond dimensions.

2. Transport in the disordered Heisenberg chain

The clear diffusive behavior observed in the transport of d bosons in Sec. IV A is not commonly observed in disordered systems. Previous studies [41,42,51] have reported slow, subdiffusive transport in the ergodic phase of disordered Hamiltonians.

In this Appendix, we explore dynamics in the disordered Heisenberg chain in a parameter range where disorder and hopping are comparable to the ones investigated in our paper. The aim of this paper is to check whether there exists a coupling strength such that the nearest-neighbor interaction of the disordered Heisenberg chain can reproduce diffusive dynamics in a similar timescale as the one observed in the main text.

Although the two-species Hubbard model and Heisenberg chain have different local Hilbert spaces, one can transform the Hubbard model to spin language to identify the comparable range of parameters. Under this transformation, the hopping t_d becomes equivalent to exchange terms that are proportional to J in the Heisenberg model, and we set $J = 1$. The random chemical potential ϵ_i acting on bosons translates to a random magnetic field $h_i = \epsilon_i/2$. Thus, we choose the Heisenberg model with the following parameters:

$$\hat{H} = \sum_i \left[\hat{s}_i^x \hat{s}_{i+1}^x + \hat{s}_i^y \hat{s}_{i+1}^y + \frac{J_z}{2} \hat{s}_i^z \hat{s}_{i+1}^z + \frac{\epsilon_i}{2} \hat{s}_i^z \right], \quad (\text{B1})$$

where $\hat{s}_i^\alpha = \sigma^\alpha/2$ are spin-1/2 operators on a given site. We set $W = 6.5$ that controls the distribution of $\epsilon_i \in [-W, W]$, and sweep through different interaction strengths J_z since nearest-neighbor interaction does not have a direct analog to the on-site Hubbard interaction. The Heisenberg model

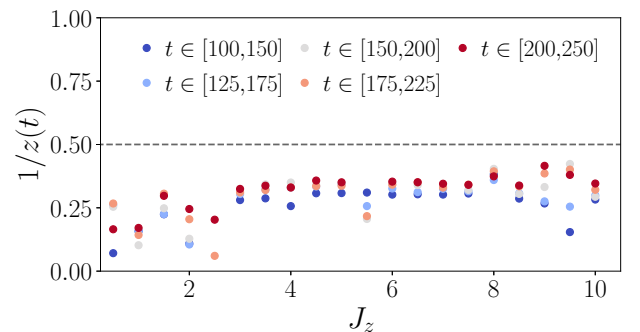


FIG. 14. The inverse dynamical exponent as a function of the interaction strength J_z . At small values of J_z , dynamics are extremely slow and oscillations complicate the estimation of $1/z$ on available timescales. For larger $J_z \geq 3$, $1/z$ shows a more regular behavior, highlighting much slower transport in the Heisenberg chain compared to the two-species Hubbard model. The data are obtained averaging over 50 disorder realizations and using a bond dimension $\chi = 256$.

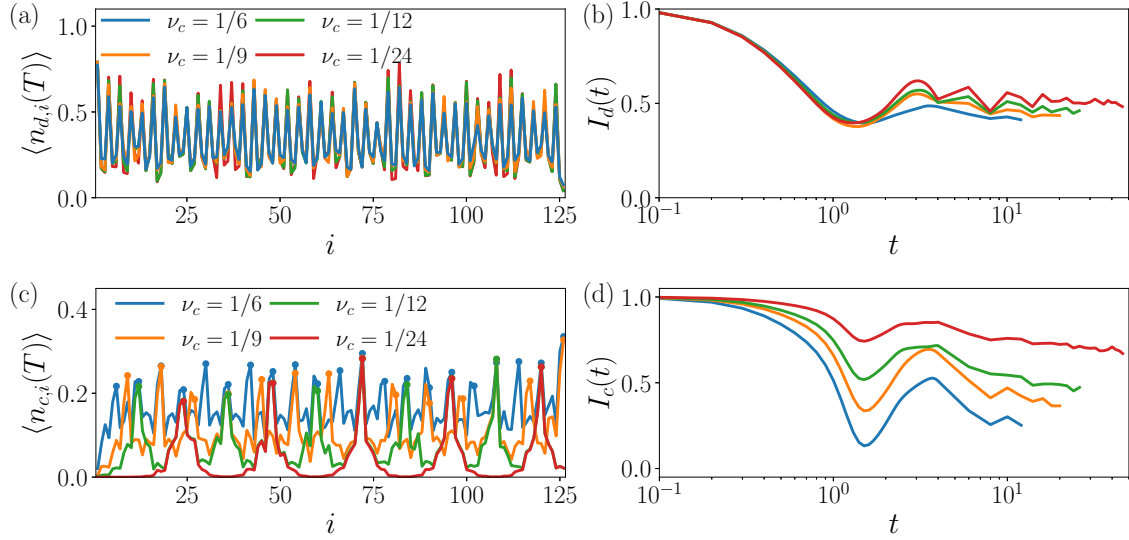


FIG. 15. The density profiles of both particle types show a clear trend, suggesting thermalization at large bath densities. However, at $\nu_c = 1/24$ $\langle \hat{n}_{c,i} \rangle$ keeps the characteristic density wave structure and the d boson density profile is significantly farther from relaxation than at larger densities. The imbalance confirms a monotonous slowdown of the relaxation towards thermal equilibrium as the bath density is decreased. The density profiles are shown at the latest time reached by the $\nu_c = 1/6$ simulation, the most expensive to simulate, $T = 16$. The value of the coupling is fixed to $U = 6$.

Eq. (B1) conserves total magnetization, allowing for the study of spin transport across a small step, in analogy with the mixed state used in Eq. (9) in the main text. A similar analysis to the one carried out in the main text results in the inverse dynamical exponent $1/z(t)$ shown in Fig. 14. The data reveal much slower transport as compared to the results of Fig. 6 in the whole parameter range explored, suggesting that the effect of the c bosons cannot be accounted for by an emergent local interaction term among disordered bosons. A possible explanation, then, is that the c bosons effectively act as a long-range interaction, justifying the faster transport observed in the two-particle species Hubbard model.

3. Dynamics at small densities of clean bosons

In the main text, we reported the deviation from logarithmic entanglement growth as a probe of delocalization at small, albeit extensive, bath size. Here we present some additional data regarding the density profiles and the imbalance, as defined in Eq. (A4).

Figures 15(a) and 15(b) show the behavior of d bosons. In Fig. 15(a), we compare the density profile for different bath densities $\nu_c \in [1/24, 1/6]$ at fixed $U = 6$ and $W = 6.5$. The relaxation of the initial density wave toward equilibrium becomes monotonously more pronounced as the density, ν_c , is increased, in agreement with the results of the main text. A similar phenomenology can be observed in the dynamics of the imbalance, which shows much faster decay at $\nu_c = 1/6$ compared to $\nu_c = 1/24$.

The bottom panels in Fig. 15 are dedicated to the c bosons. Similarly to the disordered particles, the density wave is substantially smeared at large c boson densities, while at $\nu_c = 1/24$ large regions with nearly zero density of clean bosons are visible. Figure 15(d) reveals that at every bath size ex-

plored in this paper, the imbalance of the c bosons (I_c) decays in time, although in a slower fashion at smaller bath densities.

Finally, we analyze the connected correlation function of c bosons. The data shown in the main text lead to the hypothesis that the deviation from logarithmic growth of the entanglement entropy could be generated by a significant correlation among the different c bosons. To check this hypothesis, we studied the behavior of the density-density connected correlation function among different sites l_p and l'_p , where the distance between sites l_p and l'_p corresponds to the initial position of adjacent c bosons. The results are shown in Fig. 16. The density-density correlations start growing at progressively earlier times as the density ν_c is increased and

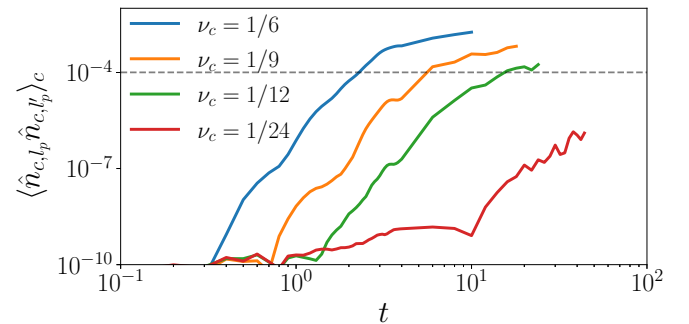


FIG. 16. Density-density connected correlations among different c bosons at fixed $U = 6$. The characteristic time at which they become larger than $\varepsilon = 10^{-4}$ defines an additional timescale $\tau_{cc}(\nu_c)$ that shows approximate power-law dependence on ν_c , $\tau_{cc} \propto 1/\nu_c^k$, with $k \approx 2.53$ for larger values of ν_c . For the smallest density $\nu_c = 1/24$, correlations may be speculated to show signatures of saturation to a value much smaller than ε , but longer times are needed to verify this hypothesis.

the correlation function crosses the threshold value $\varepsilon = 10^{-4}$ (dashed line) at a timescale τ_{cc} scaling in bath size with the same power-law observed for the onset of the deviation of entanglement growth from logarithmic. This indeed suggests that correlations among clean bosons may be responsible for

the onset of more rapid entanglement growth shown in Fig. 7 in the main text. Also, consistent with all other probes, the connected correlation function for the lowest density case, $\nu_c = 1/24$, does not cross the threshold value ε within the available simulation time.

-
- [1] A. Rubio-Abadal, J.-y. Choi, J. Zeiher, S. Hollerith, J. Rui, I. Bloch, and C. Gross, Many-Body Delocalization in the Presence of a Quantum Bath, *Phys. Rev. X* **9**, 041014 (2019).
- [2] J. Léonard, S. Kim, M. Rispoli, A. Lukin, R. Schittko, J. Kwan, E. Demler, D. Sels, and M. Greiner, Probing the onset of quantum avalanches in a many-body localized system, *Nat. Phys.* **19**, 481 (2023).
- [3] J. M. Deutsch, Quantum statistical mechanics in a closed system, *Phys. Rev. A* **43**, 2046 (1991).
- [4] M. Srednicki, Chaos and quantum thermalization, *Phys. Rev. E* **50**, 888 (1994).
- [5] M. Takahashi, *Thermodynamics of One-Dimensional Solvable Models* (Cambridge University Press, Cambridge, UK, 1999).
- [6] M. Rigol, V. Dunjko, V. Yurovsky, and M. Olshanii, Relaxation in a Completely Integrable Many-Body Quantum System: An *Ab Initio* Study of the Dynamics of the Highly Excited States of 1D Lattice Hard-Core Bosons, *Phys. Rev. Lett.* **98**, 050405 (2007).
- [7] M. Rigol, Breakdown of Thermalization in Finite One-Dimensional Systems, *Phys. Rev. Lett.* **103**, 100403 (2009).
- [8] L. D'Alessio, Y. Kafri, A. Polkovnikov, and M. Rigol, From quantum chaos and eigenstate thermalization to statistical mechanics and thermodynamics, *Adv. Phys.* **65**, 239 (2016).
- [9] N. Bondyopadhyaya and D. Roy, Dynamics of hybrid junctions of Majorana wires, *Phys. Rev. B* **99**, 214514 (2019).
- [10] M. Ljubotina, D. Roy, and T. Prosen, Absence of thermalization of free systems coupled to gapped interacting reservoirs, *Phys. Rev. B* **106**, 054314 (2022).
- [11] D. M. Basko, I. L. Aleiner, and B. L. Altshuler, Metal-insulator transition in a weakly interacting many-electron system with localized single-particle states, *Ann. Phys.* **321**, 1126 (2006).
- [12] I. V. Gornyi, A. D. Mirlin, and D. G. Polyakov, Interacting Electrons in Disordered Wires: Anderson Localization and Low- t Transport, *Phys. Rev. Lett.* **95**, 206603 (2005).
- [13] R. Nandkishore and D. A. Huse, Many-body localization and thermalization in quantum statistical mechanics, *Annu. Rev. Condens. Matter Phys.* **6**, 15 (2015).
- [14] D. A. Abanin, E. Altman, I. Bloch, and M. Serbyn, Colloquium: Many-body localization, thermalization, and entanglement, *Rev. Mod. Phys.* **91**, 021001 (2019).
- [15] R. Nandkishore, Many-body localization proximity effect, *Phys. Rev. B* **92**, 245141 (2015).
- [16] D. A. Huse, R. Nandkishore, F. Pietracaprina, V. Ros, and A. Scardicchio, Localized systems coupled to small baths: From Anderson to Zeno, *Phys. Rev. B* **92**, 014203 (2015).
- [17] S. Gopalakrishnan, K. R. Islam, and M. Knap, Noise-Induced Subdiffusion in Strongly Localized Quantum Systems, *Phys. Rev. Lett.* **119**, 046601 (2017).
- [18] K. Hyatt, J. R. Garrison, A. C. Potter, and B. Bauer, Many-body localization in the presence of a small bath, *Phys. Rev. B* **95**, 035132 (2017).
- [19] D. J. Luitz, F. Huveneers, and W. De Roeck, How a Small Quantum Bath Can Thermalize Long Localized Chains, *Phys. Rev. Lett.* **119**, 150602 (2017).
- [20] J. Marino and R. M. Nandkishore, Many-body localization proximity effects in platforms of coupled spins and bosons, *Phys. Rev. B* **97**, 054201 (2018).
- [21] N. Roy, J. Sutradhar, and S. Banerjee, Diagnostics of non-ergodic extended states and many body localization proximity effect through real-space and Fock-space excitations, *Phys. Rev. B* **107**, 115155 (2023).
- [22] S. P. Kelly, R. Nandkishore, and J. Marino, Exploring many-body localization in quantum systems coupled to an environment via Wegner-Wilson flows, *Nucl. Phys. B* **951**, 114886 (2020).
- [23] E. Wybo, M. Knap, and F. Pollmann, Entanglement dynamics of a many-body localized system coupled to a bath, *Phys. Rev. B* **102**, 064304 (2020).
- [24] M. Goihl, J. Eisert, and C. Krumnow, Exploration of the stability of many-body localized systems in the presence of a small bath, *Phys. Rev. B* **99**, 195145 (2019).
- [25] S. Nandy, F. Evers, and S. Bera, Dephasing in strongly disordered interacting quantum wires, *Phys. Rev. B* **103**, 085105 (2021).
- [26] U. Krause, T. Pellegrin, P. W. Brouwer, D. A. Abanin, and M. Filippone, Nucleation of Ergodicity by a Single Mobile Impurity in Supercooled Insulators, *Phys. Rev. Lett.* **126**, 030603 (2021).
- [27] T. L. M. Lezama and Y. B. Lev, Logarithmic, noise-induced dynamics in the Anderson insulator, *SciPost Phys.* **12**, 174 (2022).
- [28] P. Brighi, A. A. Michailidis, D. A. Abanin, and M. Serbyn, Propagation of many-body localization in an Anderson insulator, *Phys. Rev. B* **105**, L220203 (2022).
- [29] P. Brighi, A. A. Michailidis, K. Kirova, D. A. Abanin, and M. Serbyn, Localization of a mobile impurity interacting with an Anderson insulator, *Phys. Rev. B* **105**, 224208 (2022).
- [30] F. Verstraete and J. I. Cirac, Matrix product states represent ground states faithfully, *Phys. Rev. B* **73**, 094423 (2006).
- [31] P. Sierant, T. Chanda, M. Lewenstein, and J. Zakrzewski, Slow dynamics of a mobile impurity interacting with an Anderson insulator *Phys. Rev. B* **107**, 144201 (2023).
- [32] P. Ponte, Z. Papić, F. Huveneers, and D. A. Abanin, Many-Body Localization in Periodically Driven Systems, *Phys. Rev. Lett.* **114**, 140401 (2015).
- [33] A. Lazarides, A. Das, and R. Moessner, Fate of Many-Body Localization Under Periodic Driving, *Phys. Rev. Lett.* **115**, 030402 (2015).
- [34] L. Zhang, V. Khemani, and D. A. Huse, A Floquet model for the many-body localization transition, *Phys. Rev. B* **94**, 224202 (2016).

- [35] M. Sonner, M. Serbyn, Z. Papić, and D. A. Abanin, Thouless energy across the many-body localization transition in Floquet systems, *Phys. Rev. B* **104**, L081112 (2021).
- [36] P. Sierant, M. Lewenstein, A. Scardicchio, and J. Zakrzewski, Stability of many-body localization in Floquet systems, *Phys. Rev. B* **107**, 115132 (2023).
- [37] M. Müller, Purely electronic transport and localization in the Bose glass, *Ann. Phys.* **521**, 849 (2009).
- [38] I. V. Gornyi, A. D. Mirlin, M. Müller, and D. G. Polyakov, Absence of many-body localization in a continuum, *Ann. Phys.* **529**, 1600365 (2017).
- [39] J. Šuntajs, J. Bonča, T. Prosen, and L. Vidmar, Quantum chaos challenges many-body localization, *Phys. Rev. E* **102**, 062144 (2020).
- [40] D. Abanin, J. Bardarson, G. De Tomasi, S. Gopalakrishnan, V. Khemani, S. Parameswaran, F. Pollmann, A. Potter, M. Serbyn, and R. Vasseur, Distinguishing localization from chaos: Challenges in finite-size systems, *Ann. Phys.* **427**, 168415 (2021).
- [41] K. Agarwal, S. Gopalakrishnan, M. Knap, M. Müller, and E. Demler, Anomalous Diffusion and Griffiths Effects Near the Many-Body Localization Transition, *Phys. Rev. Lett.* **114**, 160401 (2015).
- [42] M. Žnidarič, A. Scardicchio, and V. K. Varma, Diffusive and Subdiffusive Spin Transport in the Ergodic Phase of a Many-Body Localizable System, *Phys. Rev. Lett.* **117**, 040601 (2016).
- [43] N. Fayard, L. Henriot, A. Asenjo-Garcia, and D. E. Chang, Many-body localization in waveguide quantum electrodynamics, *Phys. Rev. Res.* **3**, 033233 (2021).
- [44] P. W. Anderson, Absence of diffusion in certain random lattices, *Phys. Rev.* **109**, 1492 (1958).
- [45] P. W. Anderson, D. J. Thouless, E. Abrahams, and D. S. Fisher, New method for a scaling theory of localization, *Phys. Rev. B* **22**, 3519 (1980).
- [46] N. Hatano and M. Suzuki, Finding exponential product formulas of higher orders, in *Quantum Annealing and Other Optimization Methods*, edited by A. Das and B. K. Chakrabarti (Springer Berlin, 2005), pp. 37–68.
- [47] G. Vidal, Efficient Classical Simulation of Slightly Entangled Quantum Computations, *Phys. Rev. Lett.* **91**, 147902 (2003).
- [48] W. De Roeck and F. Huveneers, Stability and instability towards delocalization in many-body localization systems, *Phys. Rev. B* **95**, 155129 (2017).
- [49] R. Abou-Chacra, D. J. Thouless, and P. W. Anderson, A self-consistent theory of localization, *J. Phys. C* **6**, 1734 (1973).
- [50] M. Ljubotina, M. Žnidarič, and T. Prosen, Spin diffusion from an inhomogeneous quench in an integrable system, *Nat. Commun.* **8**, 16117 (2017).
- [51] S. Bera, G. De Tomasi, F. Weiner, and F. Evers, Density Propagator for Many-Body Localization: Finite-Size Effects, Transient Subdiffusion, and Exponential Decay, *Phys. Rev. Lett.* **118**, 196801 (2017).
- [52] M. Žnidarič, T. Prosen, and P. Prelovsek, Many-body localization in the Heisenberg xxz magnet in a random field, *Phys. Rev. B* **77**, 064426 (2008).
- [53] A. Pal and D. A. Huse, Many-body localization phase transition, *Phys. Rev. B* **82**, 174411 (2010).
- [54] V. Kravtsov, B. Altshuler, and L. Ioffe, Non-ergodic delocalized phase in Anderson model on Bethe lattice and regular graph, *Ann. Phys.* **389**, 148 (2018).
- [55] W. Tang and I. M. Khaymovich, Non-ergodic delocalized phase with Poisson level statistics, *Quantum* **6**, 733 (2022).
- [56] K. Tikhonov and A. Mirlin, From Anderson localization on random regular graphs to many-body localization, *Ann. Phys.* **435**, 168525 (2021), Special Issue on Localisation 2020.
- [57] E. V. H. Doggen, I. V. Gornyi, A. D. Mirlin, and D. G. Polyakov, Slow Many-Body Delocalization beyond One Dimension, *Phys. Rev. Lett.* **125**, 155701 (2020).
- [58] T. Thiery, F. Huveneers, M. Müller, and W. De Roeck, Many-Body Delocalization as a Quantum Avalanche, *Phys. Rev. Lett.* **121**, 140601 (2018).
- [59] A. Morningstar, L. Colmenarez, V. Khemani, D. J. Luitz, and D. A. Huse, Avalanches and many-body resonances in many-body localized systems, *Phys. Rev. B* **105**, 174205 (2022).
- [60] M. Fishman, S. R. White, and E. M. Stoudenmire, The ITensor software library for tensor network calculations, *SciPost Phys. Codebases*, 4 (2022).
- [61] H. P. Lüschen, P. Bordia, S. Scherg, F. Alet, E. Altman, U. Schneider, and I. Bloch, Observation of Slow Dynamics near the Many-Body Localization Transition in One-Dimensional Quasiperiodic Systems, *Phys. Rev. Lett.* **119**, 260401 (2017).
- [62] H. P. Lüschen, P. Bordia, S. S. Hodgman, M. Schreiber, S. Sarkar, A. J. Daley, M. H. Fischer, E. Altman, I. Bloch, and U. Schneider, Signatures of Many-Body Localization in a Controlled Open Quantum System, *Phys. Rev. X* **7**, 011034 (2017).
- [63] J. H. Bardarson, F. Pollmann, and J. E. Moore, Unbounded Growth of Entanglement in Models of Many-Body Localization, *Phys. Rev. Lett.* **109**, 017202 (2012).
- [64] M. Serbyn, Z. Papić, and D. A. Abanin, Universal Slow Growth of Entanglement in Interacting Strongly Disordered Systems, *Phys. Rev. Lett.* **110**, 260601 (2013).
- [65] V. Oganesyan and D. A. Huse, Localization of interacting fermions at high temperature, *Phys. Rev. B* **75**, 155111 (2007).